JOURNAL OF PROPULSION AND POWER
Vol. 24, No. 6, November–December 2008

Combustion of Decane-Based Slurries with Metallic Fuel Additives

E. Beloni, V. K. Hoffmann, and E. L. Dreizin
New Jersey Institute of Technology, Newark, New Jersey 07102

DOI: 10.2514/1.28042

Low-density decane-based slurries were prepared with powders of mechanically alloyed $Al_{0.7}Li_{0.3}$, nanocomposite 2B + Ti, and pure aluminum. The slurries were atomized using an ultrasonic nozzle. The aerosol was focused into a laminar vertically rising jet and ignited in air to produce a lifted flame. Combustion was studied optically. It was found that aluminum was difficult to ignite. The powders of mechanically alloyed $Al_{0.7}Li_{0.3}$ and nanocomposite 2B + Ti ignited readily and burned within the hydrocarbon flame, resulting in an increased flame temperature and length. Based on the visualized streaks, burning metal particles were well separated within the flame. The ignition of nanocomposite 2B + Ti particles was accompanied by a sharp increase in brightness and was often followed by particle microexplosions. The ignition delays of nanocomposite 2B + Ti particles were determined by the time of evaporation of liquid-fuel droplets in which metallic additives were contained. Ignition and combustion of the mechanically alloyed $Al_{0.7}Li_{0.3}$ was assisted by selective oxidation of Li. The flame length was controlled by the fuel and oxidizer diffusion rates. The flames containing mechanically alloyed $Al_{0.7}Li_{0.3}$ and nanocomposite 2B + Ti powders were longer than the pure decane flames and decane/Al slurry flames. The increased flame length indicated an additional consumption of oxidizer by metallic particles.

Introduction

ALUMINUM is widely used as an additive in various energetic formulations because of its high combustion enthalpy (e.g., [1–4]). However, for many applications, including propellants and explosives, the rate of aluminum combustion is lower than desired. Specific examples of applications in which a higher burn rate would be beneficial include aluminum additives to solid propellants [5] and enhanced blast explosives [6]. Another potential application of metallic fuel additives is in jet fuels, in which such additives can substantially increase the energy density. However, previous work on testing liquid-fuel/aluminum slurries showed that combustion of aluminum particles in this case is inefficient [6–9]. The particles were observed to agglomerate before ignition [8,9]. Once ignited, the particles burned as large agglomerates with unacceptably long burn times.

Recently, interest in metal-based high-energy-density materials was renewed with development of various related nanomaterials, which show substantial promise to achieve burn rates much higher than for regular metal powders [10,11]. One approach uses mechanical milling to produce nanostructural and nanocomposite metallic powders (e.g., [12–14]). Such powders have particle sizes on the order of several microns, comparable with the regular metal powders, but have refined structure and morphology designed to accelerate their bulk burn rates. Experimental validation of this approach was presented in [12,14–17] for several material compositions. The combustion processes of these and other similar materials are of substantial interest. A useful experimental technique was developed based on a lifted-laminar-flame aerosol burner that enabled measurement of individual particle burn rates and flame speeds in aerosols of several mechanically alloyed powders [16,18,19].

Presented as Paper 1431 at the 45th AIAA Aerospace Sciences Meeting and Exhibit, Reno, NV, 8–11 January 2007; received 15 February 2008; revision received 16 June 2008; accepted for publication 14 June 2008.

*Graduate Research Assistant. Graduate Student Member AIAA.
†Research Engineer.
‡Professor of Chemical Engineering. Associate Fellow AIAA.

However, the burner was found to be inappropriate for a range of novel materials that could not be readily handled as dry powders because of their relatively high ignition sensitivity or rapid aging in oxidizing gas environments. Specific examples are nanocomposite B-Ti powders that could be readily ignited by electric spark (whereas powder aerosols were produced in [16,18,19] using strong dc electric fields) or mechanically alloyed Al-Li powders that rapidly age in room air containing moisture. Extending the capability of studying lifted-laminar aerosol flames produced with such relatively sensitive materials was one motivation for this project. The second motivation was to investigate the combustion of metallic materials under conditions similar to those existing in many practical systems employing hydrocarbon fuels. In such systems, metallic particles ignite and burn primarily in the hydrocarbon flame, in which the primary oxidizers are CO_2 and H_2O, rather than O_2. Recently, combustion of nanocomposite B-Ti powders was studied experimentally in related $CH_4/O_2/N_2$ gas mixtures using constant-volume explosions [20]. Combustion pressures, bulk burn rates, and the overall efficiency of oxidation were assessed, but the information about individual particle combustion mechanism could not be obtained. Flame imaging and visualization of streaks of burning particles readily obtainable from the laminar-lifted-flame experiments are of great interest for the systems in which metallic particles burn in the combustion products of hydrocarbon fuels.

The goal of this project was to develop an experimental technique enabling evaluation of combustion performance for sensitive metal-based powders. It was further desired to evaluate two different types of materials and compare them with a reliable baseline, such as pure aluminum powder. Finally, the project considered the feasibility of using these newly developed high-energy-density metallic materials as additives for liquid fuels, an application shown to be impractical for aluminum powders.

Experimental

Materials

Slurries were prepared using a liquid hydrocarbon fuel with a metal-based fuel additive. The hydrocarbon used in these experiments was decane by Fluka (specified purity better than 95%). Decane was chosen because it is a major component of jet fuels. Metallic additives included a nanocomposite powder with bulk composition, 2B + Ti, a mechanically alloyed powder with equivalent chemical formula, $Al_{0.7}Li_{0.3}$, and a pure aluminum powder. Figure 1 shows the particle size distributions for the powders used in these experiments. These size distributions were measured by

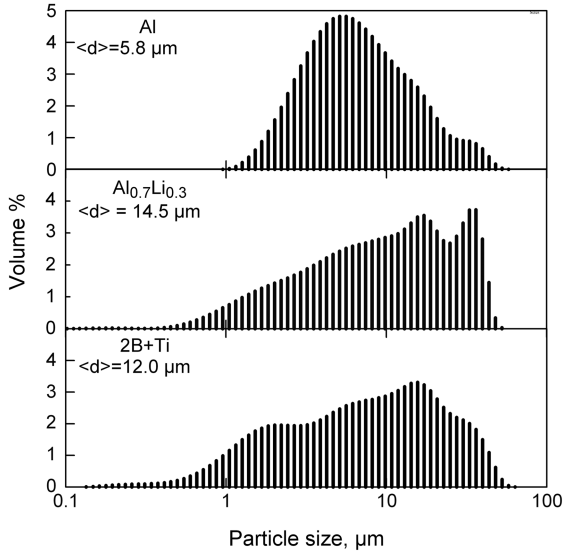

Fig. 1 Particle size distributions for Al, mechanically alloyed $Al_{0.7}Li_{0.3}$, and nanocomposite 2B + Ti powders used in this research.

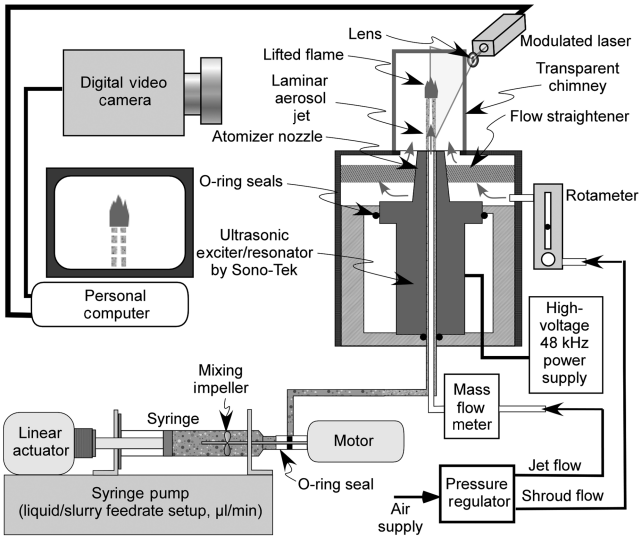

Fig. 2 Experimental setup for flame measurements for hydrocarbon fuel-metal slurries.

low-angle laser light-scattering using a Beckman-Coulter LS230 enhanced particle analyzer. The volume mean particle diameter for aluminum is the smallest, but the size distributions are generally broader for both powders produced by mechanical milling.

The preparation of nanocomposite 2B + Ti by arrested reactive milling is described in [14]. The elemental components of the nanocomposite are not bonded chemically. When this material is heated, a highly exothermic reaction $2B + Ti \rightarrow TiB_2$ is expected to occur nearly simultaneously along the entire reactive interface between B and Ti. Because this interface is highly developed and because the mixing between components is uniform throughout the volume of each micron-sized particle, the B-Ti reaction is expected to heat the particles rapidly and uniformly. This heating is expected to reduce the ignition delay substantially.

Procedures used to produce mechanically alloyed $Al_{0.7}Li_{0.3}$ powder are also described elsewhere [21]. This alloy is expected to ignite much more readily than pure aluminum because of selective oxidation of Li, beginning at fairly low temperatures [22].

Aluminum powder was 99.9% pure, with nominal particle sizes in the range of 1–5 μm, by Atlantic Equipment Engineers. It served as a reference point for assessment of the performance of other metal-based fuels.

Lifted-Laminar-Flame Slurry Burner

The experimental approach employing a lifted-laminar-flame aerosol burner described in [16,18,19] and designed to characterize combustion of solid-fuel aerosols was further developed here to work with liquid and slurry fuels. A schematic diagram of the experimental setup is shown in Fig. 2. The burner is built based on a model 8700-48M, 48 kHz Sono-Tek ultrasonic atomizer with a dual microbore. The diagram of the atomizer nozzle with respective dimensions is shown in Fig. 3. The liquid is fed through a channel within the atomizer body, and the amplitude of the ultrasound is at its maximum at the top of the nozzle. A coaxial central gas channel is built into the liquid-fuel channel of the atomizer, so that the aerosol produced around the circumference of the nozzle is entrained into a vertically rising central gas jet. Therefore, a small-diameter laminar aerosol jet is produced. The central air jet was used in all experiments described here, although other gases can be used to simulate different combustion environments. Immediately at the nozzle, the liquid or slurry droplets are concentrated in a ring around the jet circumference; the droplets are distributed more uniformly within the jet at longer distances from the nozzle. Air is fed into the central jet through a pressure regulator and is monitored using an Alicat Scientific mass flow meter. A slow shroud gas flow is provided that serves two purposes: it stabilizes the aerosol jet and provides

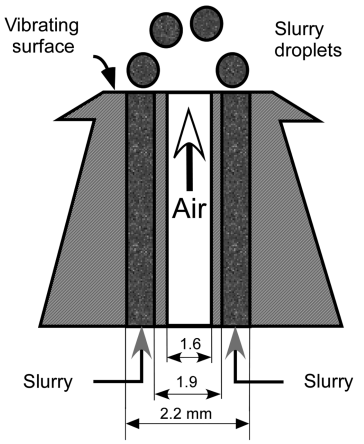

Fig. 3 Atomizer nozzle design and dimensions.

additional oxidizer to the flame, because the oxygen contained in the central air jet is insufficient for the stoichiometric combustion. The shroud gas flow is metered using a rotameter. A metered flow of the liquid fuel or slurry is fed to the burner using a Genie Plus syringe pump. A polycarbonate syringe is used with a custom-made aluminum plunger that is inert in the hydrocarbon fuel environment. A custom-made spinning impeller is placed inside the syringe. It is connected to a shaft of a dc motor and used to ensure homogeneous slurry fed from the syringe to the burner.

Once a laminar jet is established, a flame is ignited. The lifted-flame structure for the produced slurry droplets is comparable with that of the flames produced with solid particles [16,18,19]. As in [16,18,19], the rising aerosol jet decelerates and the flame is stabilized at a location at which its velocity (directed down) is equal to the upward jet speed. As the slurry ignites, the liquid fuel evaporates and burns, whereas the metallic additive initially remains encapsulated in the boiling decane droplets. When metallic particles are exposed to a hot oxidizing environment, they can ignite and burn themselves. Metallic particles burn with mixed oxidizers, including combustion products of decane and oxygen diffusing from the flame surroundings.

Produced slurries contained 20 wt % of a metal additive. This mass loading was selected based on preliminary tests showing that at greater concentrations, metal powders tend to agglomerate before atomization. Based on the nominal particle sizes (cf. Fig. 1) and nominal diameter of the produced liquid droplets (38 μm), it was estimated that this loading level corresponded to only 1–3 metallic particles per droplet.

Flame Speed Measurements

The aerosol jet is illuminated using a vertical laser sheet so that the moving droplets scatter the light and are well visible. A 20 mW Shanghai Uniwave Technology DPGL-3020 model laser with a wavelength centered at 532 nm is used. The laser irradiation is modulated (usually at 1000 Hz) so that the droplet trajectories appear as dashed lines and the period of the dashed pattern is used to determine the jet speed. The jet speed measured immediately before the flame front was assumed to be equal to the flame speed. The velocity slip between decane (or slurry) droplets and the gas jet was neglected. It was estimated that for a decane droplet, the velocity relaxation time

$$\tau = \frac{\rho D^2 C_C}{18\upsilon} \approx 3.9 \text{ ms} \quad (1)$$

where decane density $\rho = 730$ kg/m^3 [23], droplet diameter $D = 38$ μm (nominal initial diameter for the nozzle used), ν is the kinematic viscosity of air at room temperature, and C_C is the Cunningham slip correction factor calculated for a liquid droplet [24]. Because hydrocarbon droplets evaporate quite readily even at room temperature, the initial diameter of the droplets entering the flame is expected to be significantly smaller than their nominal initial diameter. Therefore, an estimate of the relaxation time based on the initial droplet diameter is conservative and the actual relaxation times are smaller. Note also that the gravity force was estimated to be of the order of only 2% of the drag force exerted on the droplet in the rising jet. Thus, the effect of gravity on the droplet velocity was also negligible. Based on the measured droplet velocities, the time the droplets moved from the nozzle to the flame is estimated to be close to or greater than 7 ms, justifying the assumption of the negligible velocity slip.

Flame Imaging

A Panasonic 3 charge-coupled device camcorder was used in the flame imaging. The camcorder was mounted on a stand with the lens placed 10.2 cm from the burner. The video feed was captured and processed with Motion DV Studio software. The camcorder zoom was set such that the viewed frame height was about 15.9 mm. For a stable flame, several minutes of video were typically recorded to ensure that characterization of the flame could be conducted. Figure 4 shows a typical frame image obtained and shows the specific parameters determined from the image analysis. Image processing software packages ImageTool [25] and Tracker [26] were used. For each slurry, at least 14 characteristic frames were chosen from which the measurements of the jet speed were made using particle image velocimetry. In addition, the length of the soot region (cf. Fig. 4) was measured for each slurry combustion experiment using the same flame images.

Measurements of the flame length and its height above the burner were made using at least 500 images. To determine the flame length, two areas were selected in the flame video image within the Tracker window: one area included the leading edge of the flame and the other included its trailing edge. Threshold tracking was used so that the selected areas automatically followed displacements of the leading and trailing edges of the flame from frame to frame. The position of the area tracking the flame's leading edge was used to determine the flame height. The distance between the two areas was recorded and represented the varying flame length.

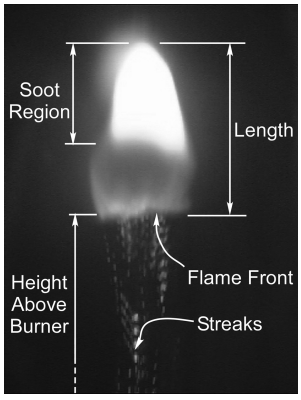

Fig. 4 Typical flame image for the pure decane jet; parameters and characteristics determined by the flame image analysis are shown.

Flame Emission Measurements

An EPP2000C fiber optic spectrometer by StellarNet, Inc. was used to capture the flame emission spectra. The spectrometer works in the wavelength range of 190–850 nm with ~0.5 nm resolution. The spectrometer input was coupled to a fiber optics cable. The fiber optics cable was mounted on a 2-D micropositioner and was placed 38 mm from the burner. Once a stable flame was produced, the fiber optic cable's vertical position was adjusted to line up with the flame. Spectrawiz software was used in the acquisition of spectra.

The diameter of the field of view of the spectrometer was 6 mm. It was determined in a separate experiment. In that experiment, an image was produced by a collimated laser diode beam directed on a white light-scattering surface. The input window of the fiber optic cable connected to the spectrometer was placed 38 mm away from the image. The cable was moved up and down, parallel to the light-scattering surface, and the intensity of the signal recorded by the spectrometer was determined as a function of the fiber optic cable position. The field of view was defined as a width of the obtained bell-shaped curve measured at half of its maximum. It is comparable with the dimensions of the flames addressed in this project; therefore, the recorded spectra represented an integrated flame emission, rather than the emission from a specific region of the flame.

The spectrometer was calibrated using a Thorlabs tungsten strip-filament lamp and a horizontal slit aperture blocking emission from the uncalibrated portions of the lamp's filament. The linearity calibration was performed using Edmund Industrial Optics gray step filters. The filtered emission from the strip lamp was measured simultaneously by the spectrometer and by a Thorlabs photodiode. Because of significant differences in the gray-body emission intensity at ultraviolet and visible portions of the spectrum, two different strip-lamp current settings (and, respectively, two different filament temperatures) were used for the spectrometer calibration to cover both spectrum ranges. To enable quantitative interpretation of the recorded spectra (e.g., for the optical pyrometry), calibration coefficients were obtained for each subrange of the discretized spectrum recorded by the spectrometer. Each calibration coefficient was the ratio of the emission intensity calculated using Stefan–Boltzmann's law for a blackbody emitter corrected by the tungsten emissivity [27] and the respective spectral intensity measured for the tungsten filament. For all of the calibration measurements, the spectrometer acquired individual spectra integrated over 47 ms with 10 spectra collected and averaged for each measurement.

For each flame emission measurement, 100 spectra were collected using the same integration time for each individual spectrum. Because the flame position oscillated about its stable location, the intensity of the recorded spectra could change substantially over the acquisition time. To choose the spectra representing a stable flame location, the spectral count for a wavelength of 700.1 nm was chosen to avoid major molecular lines. The spectral count at 700.1 nm was plotted as a function of time for each set of 100 spectra. The time intervals during which the spectral count remained nearly constant were selected and the following spectrum processing was performed using at least 3 consecutive spectra.

The averaged spectra were multiplied by the calibration coefficients to produce the effective emission intensity. Characteristic spectra for each type of flame studied in this work are shown in Fig. 5 and discussed subsequently. The respective emissivities for the spectra shown in Fig. 5 were normalized to enable plotting all the spectra in the same vertical scale. The spectral patterns were also shifted vertically for this presentation. Effective gray-body temperature was determined for each spectrum by matching it with a respective curve calculated using the Stefan–Boltzmann radiation

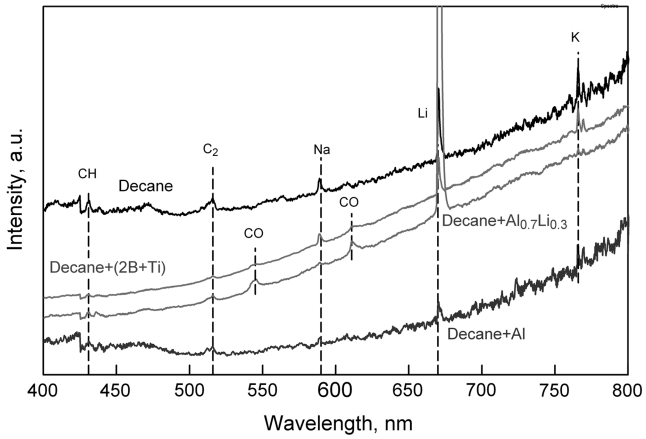

Fig. 5 Spectra measured for the flames of decane and decane-based slurries; emission peaks for CH, CO, and C_2 and for Li, K, and Na are identified based on [28,29], respectively.

law. The curve-fitting was performed with a 95% confidence interval. For this curve-fitting, specific emission peaks were identified and removed manually from the measured spectra.

Results

For the decane flame and for all slurries, the liquid feed rate was set at 70 μL/ min. The shroud flow rate was set at 1.5 L/ min. The power for the ultrasonic nozzle was set to 5 W. The central jet flow rate, adjusted in each experiment to produce a stable flame, was varied between 160 and 195 cm^3/ min. The slurries produced candlelike flames with a fairly well-defined flat flame front (i.e., the leading edge of the flame visible at the bottom of each image). An image shown in Fig. 4 represents the characteristic shape of a decane flame with a clearly visible, relatively flat flame front, followed by soot-free and soot-forming regions. No coarse condensed combustion products formed in these experiments, and the produced smoke readily penetrated through a filtering paper placed above the flame. The bulk of the deposit collected on the filtering paper in selected experiments was soot. In addition, unburned droplets were collected on silicon wafers. The wafers were examined under a microscope after allowing the decane to evaporate. As expected, only 1–3 particles were observed to remain in the regions in which the droplets landed.

Flame Speed

The flame speeds determined from the particle image velocimetry for the droplets entering the flame front varied from about 41 to 61 cm/s. These speeds are typical for hydrocarbon flames. Specific values for the measured speeds (as well as other flame parameters discussed subsequently) are shown in Table 1. The error range shown represents the standard deviation for the experimental data. No clear effect of the metallic additive on the flame speed could be detected. Both preset central air flow rate and measured flame speed are shown in Table 1. In each experiment, the air flow rate was adjusted to obtain a stable lifted flame. Generally, higher central air-jet flow rates corresponded to somewhat higher measured flame speeds, which, however, did not hold true for the Al-filled slurry. Note that the observed variation in the flame speed was rather small and generally comparable with the obtained error range.

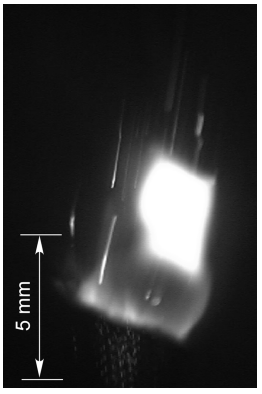

Fig. 6 Typical flame image for 2B + Ti–decane and decane flame envelope are visible.

Flame Images: Streaks of Burning Particles

For each slurry, metal-particle combustion streaks were observed. Figure 6 shows a characteristic image for a flame produced by the 2B + Ti/decane slurry. Multiple streaks are seen to originate in the flame, with particles continuing to burn inside or even outside of the decane flame envelope.

For the 2B + Ti slurry, the particle streaks typically originated from a soot-free region, close to the flame front, as can be seen from Fig. 6 and as is better illustrated in Fig. 7. The edge of the decane flame is visible at the bottom of each image fragment of Fig. 7. The left fragment shows a streak originating from a bright area. The right image fragment shows only the beginnings of two streaks. The streaks themselves did not appear in the image, most likely because the particles ignited by the end of the video-image exposure time. The distances from the flame leading edge to such bright regions indicating ignition locations for 2B + Ti nanocomposite particles were measured for a set of video images. The results of this measurement are presented in Fig. 8. The mode of the shown bell-shaped curve is at about 1.6 mm, which corresponds to an ignition delay of about 2.9 ms for a flame speed of 54.3 cm/s for this experiment.

Recorded images showed that some of the nanocomposite particles exploded shortly after their ignition. An example of a typical magnified image fragment is shown in Fig. 9. The initial bright streak separates into several individual streaks showing combustion of the particle fragments produced in such a microexplosion.

For the flames produced with the $Al_{0.7}Li_{0.3}$ slurry, flame images were dominated with bright red color, indicative of the characteristic Li emission. Figure 10 shows a typical flame image for a slurry of $Al_{0.7}Li_{0.3}$/decane. Multiple particle streaks are produced and clearly visible. The streaks are not as bright or sharp as for the 2B + Ti nanocomposite particles discussed already. Also, particle ignition locations cannot be clearly identified. The image shown in Fig. 10

Table 1 Summary of measured parameters for different slurry flames

Slurry	Central jet flow rate, cm^3/ min	Flame speed v, cm/s	Flame length l, mm	Combustion time $t = l/v$, ms	Soot/total length ratio	Temperature, K
Decane	170	56.4 ± 4.7	7.1 ± 2.4	12.6 ± 8.7	0.504	2153
	180	59.3 ± 8.3	6.3 ± 4.0	10.5 ± 8.3	0.495	2131
Decane + Al	160	49.9 ± 6.9	5.8 ± 2.0	11.6 ± 6.7	0.483	1789
	175	41.1 ± 10.1	8.0 ± 2.4	19.5 ± 4.8	0.571	1867
Decane + $Al_{0.7}Li_{0.3}$	175	49.8 ± 7.1	8.2 ± 2.5	16.5 ± 3.1	0.659	2421
	195	60.8 ± 14.6	7.5 ± 4.0	12.3 ± 6.9	0.608	2126
Decane + 2B + Ti	160	45.0 ± 5.6	10.4 ± 2.7	23.1 ± 3.4	0.519	2412
	175	54.3 ± 7.0	8.7 ± 3.0	16.0 ± 5.0	0.479	2164

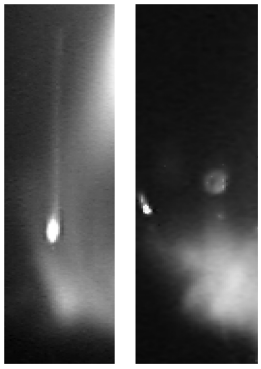

Fig. 7 Magnified fragments of the 2B + Ti slurry flame images showing the bright regions corresponding to particle ignition; the entire fragment height is 5 mm for each image.

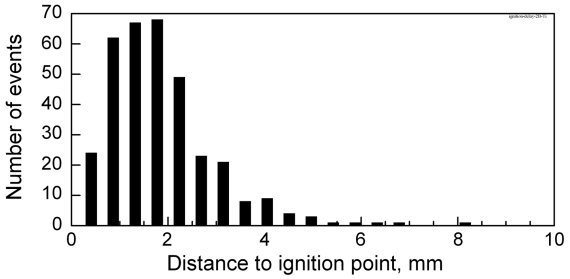

Fig. 8 Distance from the decane flame front to ignition regions of the 2B + Ti nanocomposite particles; respective flame speed is 41.5 m/s.

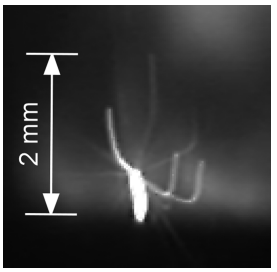

Fig. 9 Magnified fragment of a 2B + Ti slurry flame image showing a microexplosion of a nanocomposite particle following its ignition.

does not show a clearly outlined soot region, as seen in Figs. 6, 7, and 9. The soot regions were observed to appear and disappear in the experiments with the $Al_{0.7}Li_{0.3}$/decane slurry. In many images, two or even three separated soot regions were observed to form. Such separate soot regions could be positioned in parallel (above the flame

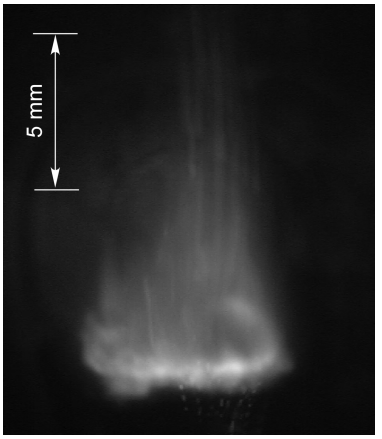

Fig. 10 Typical flame image for the $Al_{0.7}Li_{0.3}$–decane slurry. Multiple streaks of burning particles are visible.

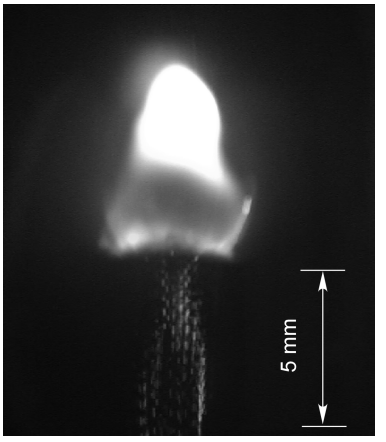

Fig. 11 Typical flame image for Al–decane slurry; a particle streak is visible on the right side of the image.

front) or in series, one on top of another. Particle streaks predominately began within the soot-free portion of the flame.

A characteristic image for the flame produced by combustion of Al/decane slurry is shown in Fig. 11. There were very few particle streaks observed. The streaks that were detected most often were at the flame's periphery. An example of such a streak can be seen on the right side of the flame shown in Fig. 11. The streak starts almost at the flame leading edge and becomes brighter about 2 mm above, before disappearing. Sometimes, as in the case of $Al_{0.7}Li_{0.3}$ slurry, parallel soot-producing regions were observed.

Flame Images: Length

The results of the flame length measurements are presented as histograms in Fig. 12. For each histogram shown in Fig. 12, the mode was determined as the most probable flame length; these lengths are shown in Table 1. The error ranges represent the standard deviations for the experimental data. The flame lengths were essentially the same for decane and Al/decane slurries, whereas for the slurries with mechanically alloyed $Al_{0.7}Li_{0.3}$ and nanocomposite 2B + Ti

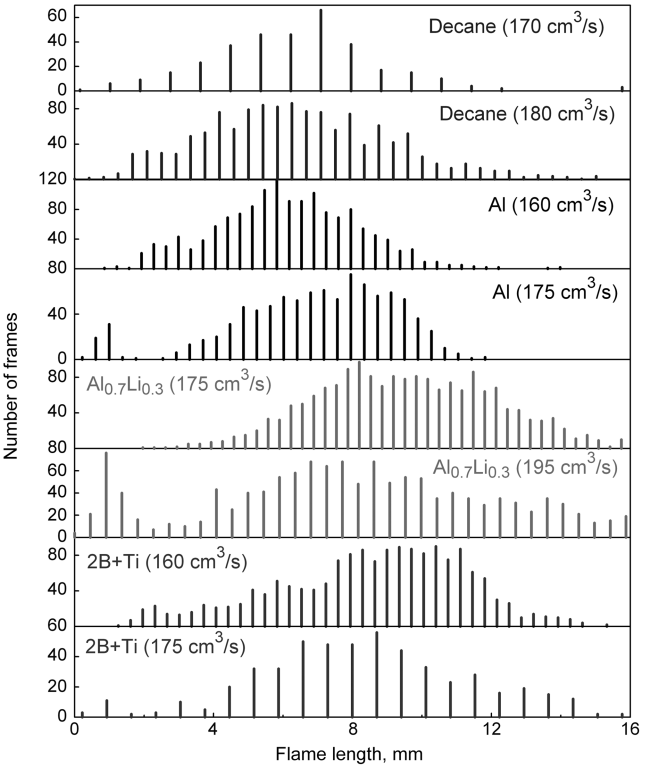

Fig. 12 Flame length distributions for different slurries; respective central jet air flow rates are shown for each histogram.

powders, the flames became longer. The flame length distribution was the narrowest for the Al/decane slurry at the fuel feed rate of 160 cm^3/ min. On the other hand, the widest distribution was observed for the flames with $Al_{0.7}Li_{0.3}$/decane slurry.

A weak correlation between the flame length and its vertical location was observed for all flames. The correlation was especially noticeable at smaller central jet air flow rates. An example of such a correlation for the pure decane flame is shown in Fig. 13. The flame's vertical location is related to its speed because the fuel jet decelerates as it is rising vertically. Because the particle image velocimetry measurements were performed manually, the flame speed was not determined from as many images as were used for measurements of the flame length and its vertical location. Therefore, the flame vertical position could serve as a convenient and qualitative indicator of its speed determined from a statistically more representative set of images. Detailed measurements of the jet velocity as a function of height were outside of the scope of this work.

Generally, higher flame speeds corresponded to their lower vertical positions. Thus, the correlation shown in Fig. 13 indicates that the faster flames were generally somewhat shorter than the slower flames. The maximum burn times for the slurry droplets were estimated from the ratio of the flame length to its speed. These times, shown in Table 1, vary from about 10 to 23 ms. An additional parameter related to the flame length is the ratio of the length of the sooting flame portion to its entire length. This parameter, also shown in Table 1, is close to 0.5 for all the flames except for the $Al_{0.7}Li_{0.3}$ slurry, for which it is noticeably greater and exceeds 0.6.

Flame Emission and Temperatures

Figure 5 shows spectral intensities measured for different flames. The strongest identifiable lines are produced by Li, K, and Na [28]. The emission produced by Li is clearly the strongest for the $Al_{0.7}Li_{0.3}$ slurry flame. However, it is also present as a much weaker line in the other spectra, indicating the presence of minor Li impurity that was not removed from the liquid flow system despite its thorough cleaning. Similarly, the lines produced by Na and K are often observed and indicate minor impurities present in the fuel. Molecular emission bands were identified as produced by CH, C_2, and CO [29]. No molecular bands attributable to the emission of boron or aluminum oxides could be unambiguously identified. The absence of aluminum and boron oxide emission signatures indicates that the vapor-phase combustion was not prominent for either of the materials. Note, however, that the boron boiling temperature (4200 K) is substantially higher than its adiabatic-flame temperature, and so its combustion is expected to occur primarily on the particle surface.

The overall slope for each of the shown spectra closely follows a corresponding thermal gray-body emission envelope. For the pure decane and Al slurry flames, the slopes are generally lower, indicating lower temperatures than for the flames of $Al_{0.7}Li_{0.3}$ and 2B + Ti slurries. The highest flame temperatures exceeding 2400 K were observed for the slurries with mechanically alloyed $Al_{0.7}Li_{0.3}$ and nanocomposite 2B + Ti powders. In general, for each slurry, with the exception of Al, higher temperatures were observed at lower central jet flow rates (cf. Table 1).

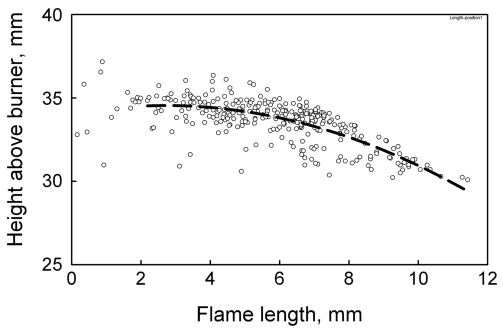

Fig. 13 Correlation between the vertical flame position and the flame length for decane flame at the central jet air flow rate of 170 cm^3/s.

Theoretical flame temperatures versus equivalence ratio were calculated using the Chemical Equilibrium with Applications (CEA) code [30]. The calculations were performed at a constant pressure equal to 1 atm. For each slurry, two fuel compositions were considered. For one composition, the solid additive concentration corresponded to 20 wt % of solid, as used in the experiments. The second concentration corresponded to 50 wt % of solid and was considered to evaluate the sensitivity of the flame temperature to the solid load. In addition, increased effective solid loads were expected in the flames after initial evaporation and combustion of decane occurring before the ignition of metal particles. A calculation aimed to consider a case when metal fuel additive did not burn at all was also considered. To assess the effect of aluminum as a heat sink, a case with 20 wt % of Al was calculated with all the Al-based oxides, carbides, and hydroxides disallowed to form. In calculations, the fuel (including both decane and solid additive) to oxygen equivalence ratios varied from 0.5 to 1.5. The results of all calculations are presented in Fig. 14. It is predicted that using 20 wt % of a metallic additive results in a slight increase of the adiabatic-flame temperature. This effect becomes more significant, especially for Al, when the concentration of the metallic additive is increased to 50 wt %. The predicted increase in the adiabatic-flame temperature is least significant for the 2B + Ti composition because of the relatively low saturation temperature for B_2O_3 and respective formation of gaseous species (e.g., BO, HBO, BO_2, B_2O_2, and others).

For each flame, the experimental temperatures (cf. Table 1) are also shown in Fig. 14. The experimental temperatures are shown as bands covering the entire range of the presented equivalence ratios. This presentation reflects an estimated broad range of equivalence ratios that could occur in the experiments: from 2.5–3.5, calculated assuming that combustion involves only the central jet air, to 0.3–0.35, obtained assuming that the both central jet air and the shroud air were available for combustion. The vertical size of the shown band represents the difference in the flame temperatures measured in repeated experiments with somewhat different central jet flow rates and, respectively, different flame speeds, as shown in Table 1. The flame temperature for decane was very reproducible and quite close to the maximum adiabatic-flame temperature of 2265 K at equivalence ratio 1. The temperatures for the flames of aluminum slurry were quite low and noticeably lower than even the maximum adiabatic-flame temperature for such a slurry, in which aluminum is inert. The temperatures measured for the slurry flames containing mechanically alloyed $Al_{0.7}Li_{0.3}$ and nanocomposite 2B + Ti powders varied in wider ranges but generally exceeded both experimental and theoretical maximum adiabatic-flame temperature for the pure decane. They were reasonably close to the calculated maximum adiabatic-flame temperatures for the respective slurries, as shown in Fig. 14.

Discussion

Flame Speed and Temperature

The reported flame speeds for premixed decane–air flames are in the range of 20–80 cm/s for a range of equivalence ratios of 0.6–1.4 [31]. The higher flame speeds occur for preheated fuel jets. The flames produced in this work were only partially premixed and not preheated. Therefore, the expected flame speeds would be at the lower end of those reported in the literature range. The speeds measured here for the decane–air flames were in the range of 56–59 cm/s and varied only slightly at the change of the central air-jet flow rate. The flame speeds for slurries varied in the range of 41–60 cm/s, which is very close to the similarly produced flames for decane without metallic additives. For Al–decane slurries, the flame speeds were somewhat lower than for the pure decane. This effect is generally consistent with other observations, including reduced flame temperature and absence of multiple particle streaks, suggesting that the bulk of aluminum particles did not burn. Thus, for this specific case, the added metal powder served as an extra heat sink that cooled and slowed down the decane flame. For the cases of nanocomposite 2B + Ti and mechanically alloyed $Al_{0.7}Li_{0.3}$ powder

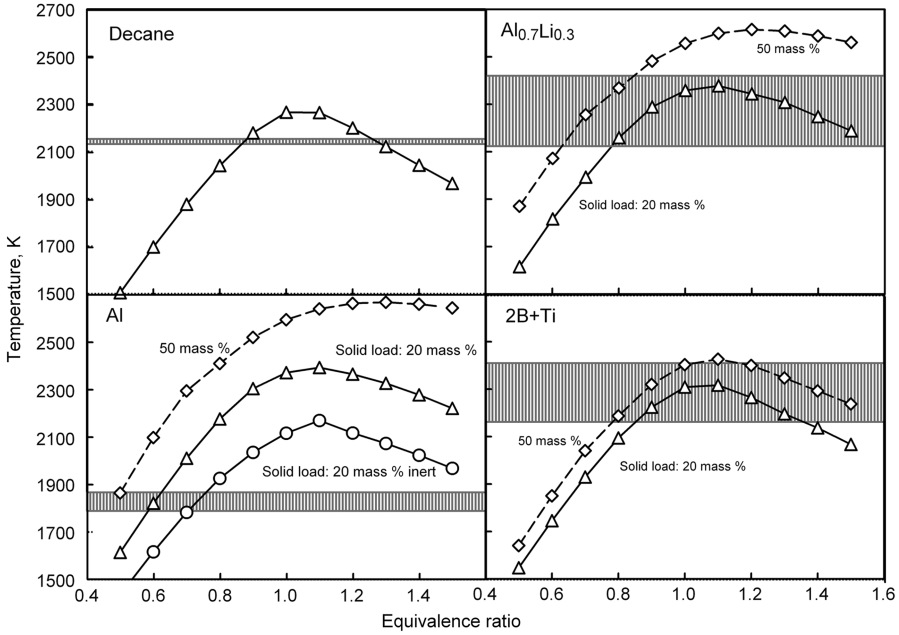

Fig. 14 Experimental flame temperatures (bands, see text and Table 1) and calculated adiabatic-flame temperatures for different fuels plotted versus equivalence ratio.

additives, no substantial effect on the flame speed was observed. At the same time, the flame temperatures were somewhat higher than for the pure decane, indicating a nonnegligible contribution of heat release from metal combustion. A correlation between the flame speed and flame temperature is noticeable from data shown in Table 1. For all the flames except for Al–decane slurry, higher flame temperatures corresponded to lower central jet feed rates and, respectively, lower flame speeds. This correlation can be interpreted considering processes of mixing the central fuel-rich jet with the shroud air flow. With the lower central jet velocities, the region with a stoichiometric mixture is less elongated and more compact. Therefore, the effect of heat losses is smaller and the flame temperature becomes higher. The lower flame speeds correlated with greater ratios of the length of the soot region to the entire flame length.

Flame Length

The experimental flame lengths were compared with those estimated using Roper's empirical correlation for diffusion flames produced over a circular port [32]. The expression used for the flame length L was

$$L = 1330 \frac{Q_F (T_\infty / T_F)}{\ell_n (1 + 1/S)} \tag{2}$$

where Q_F is the fuel volumetric flow rate; T_∞ and T_F are the oxidizer and fuel stream temperatures, respectively; and S is the stoichiometric molar oxidizer/fuel ratio. This formula is derived for gaseous fuels, and so to determine the fuel flow rate in this case, when fuel comprises condensed decane droplets and metal particles, the flow rate was calculated considering pyrolysis of decane. A thermodynamic equilibrium calculation was performed using the CEA code to determine the number of moles of gas produced by the decane pyrolysis at its boiling temperature. It was found that 1 mol of decane produces about 4.93 mol of gaseous hydrocarbon species, mostly CH_4. The values of T_∞ and T_F were assumed to be 300 and 447 K, respectively. The values of stoichiometric molar oxidizer/fuel ratios S_{pure} were initially calculated for stoichiometric combustion of decane with a specified amount of each of the metal additives corresponding to 20 wt %. However, this value was different from S, which should be used in Eq. (2) when part of the oxidizer is coming with the fuel jet, as was the case in these experiments because of the central jet air flow. A correction for S is recommended to account for this primary aeration [32]:

$$S = \frac{1 - \psi}{\psi + (1/S_{\text{pure}})} \tag{3}$$

where ψ is the percentage of the primary aeration of air in the fluid stream. The value of ψ was calculated for each fuel used, and the final values for S and for the obtained flame lengths are shown in Table 2.

The estimated and measured flame lengths are reasonably close to each other, indicating that the discussed approach is reasonable for considering the produced flames as controlled by diffusion. Although changes in the flame length predicted by Eq. (2) as a function of the central air flow rate are smaller than experimental observations, the predicted correlation between smaller flow rates and shorter flames is generally observed.

The increased flame lengths observed for the $Al_{0.7}Li_{0.3}$/decane and 2B + Ti/decane slurries can be explained by the active additional consumption of oxidizer by metallic additives. Metal combustion occurs around particles concentrated around the central portion of the flame. Therefore, effectively higher fuel concentrations are produced at the center of the jet and, respectively, longer diffusion flames are formed.

Combustion of Metallic Additives

Mechanically alloyed $Al_{0.7}Li_{0.3}$ powders and nanocomposite 2B + Ti powders added to decane burned as individual particles, producing multiple but well-separated streaks and resulting in an increased flame temperature. On the other hand, aluminum particles

Table 2 Calculated and experimental flame lengths

Slurry	Central air flow rate, cm^3/s	Measured flame length, mm	Calculated flame length, mm	S
Decane	170	7.1 ± 2.4	11.8	2.02
	180	6.3 ± 4.0	11.6	1.88
Al	160	5.8 ± 2.0	11.1	2.03
	175	8.0 ± 2.4	10.9	1.82
$Al_{0.7}Li_{0.3}$	175	8.2 ± 2.5	10.7	1.78
	195	7.5 ± 4.0	10.4	1.54
2B + Ti	160	10.4 ± 2.7	11.8	2.08
	175	8.7 ± 3.0	11.4	1.87

generally did not burn, despite their smaller average particle size, as shown in Fig. 1. No substantial particle agglomeration was observed based on both flame images, showing individual particle streaks, and collected combustion products that did not contain coarse particles.

The low efficiency of aluminum combustion in a slurry is generally consistent with previous reports [6,8,9]. It is also interesting that most of the aluminum-particle streaks were observed at the flame periphery, suggesting that aluminum particles ignited in air but not in the environment comprising products of pyrolysis and combustion of decane.

The clearly visible bright areas indicating ignition of the 2B + Ti particles confirm the proposed mechanism of their ignition boosted by the highly exothermic reaction between B and Ti [14]. Such a reaction occurs very rapidly and, essentially, throughout the entire volume for each nanocomposite particle. It causes a rapid particle heating followed by its ignition in the external oxidizer. Furthermore, particle microexplosions occurring early in their combustion were observed directly for the first time. Such microexplosions indicate that the relatively coarse nanocomposite powders are capable of very rapid burn rates as a result of forming much finer reactive particles immediately upon ignition.

The ignition delays for the 2B + Ti nanocomposite particles, determined based on the locations of the initial bright spots from which the particle streaks initiated, were estimated to vary around 3.9 ms. This time is substantially longer than the time required to heat a small metallic particle to its ignition temperature in the hot-gas environment, even if the ignition temperature is assumed to be close to 2000 K. On the other hand, this time can be compared with the time required to evaporate (burn) a decane droplet containing metallic particles. The evaporation time can be estimated as [32,33]

$$\tau = \frac{D^2}{(8k/\rho C_p)\,\ell_n(1+B)} \tag{4}$$

where D is the droplet diameter; k is thermal conductivity of gas; ρ and C_p are decane density and specific heat, respectively; and B is the transfer number, which is close to 8.4 for decane combustion in air [33]. For the initial droplet diameter $D = 38\ \mu$m, the burning time is close to 5.8 ms. The time of 3.9 ms corresponds to combustion of a droplet of about a 31 μm diameter. Thus, it is likely that part of the decane is evaporated before the slurry droplet enters into the flame and the ignition delay for metallic additives is controlled by the evaporation of the leftover liquid.

The combustion behavior of mechanically alloyed $Al_{0.7}Li_{0.3}$ powders is also in general agreement with the reaction mechanism expected for that material. Ignition is predicted to be triggered by selective oxidation of Li, resulting in continuous particle heating and combustion of Al [21,22]. The brightly colored red streaks indicate the presence of Li vapor during particle combustion and not only upon its ignition. Thus, Li oxidation supports accelerated ignition and, furthermore, affects the bulk burn rate of the mechanically alloyed particles.

Conclusions

A new experimental technique was developed for characterization of combustion of metal-based high-energy-density materials used as additives to hydrocarbon fuels. The experiments with decane and decane-based slurries containing pure Al, mechanically alloyed $Al_{0.7}Li_{0.3}$ powders, and nanocomposite 2B + Ti powders were performed. It was observed that the bulk of aluminum powder did not burn in the produced flames and most of the ignited aluminum particles were detected only at the peripheral regions of the flame reach with oxygen. On the other hand, combustion of mechanically alloyed $Al_{0.7}Li_{0.3}$ and nanocomposite 2B + Ti powders was clearly established based on both multiple particle streaks and elevated measured flame temperatures. The ignition of nanocomposite 2B + Ti particles was accompanied by rapid heat release and was often followed by the microexplosions of ignited particles. The ignition delays of nanocomposite 2B + Ti particles were determined by the time of evaporation of liquid-fuel droplets in which metallic additives were contained. Ignition and combustion of the mechanically alloyed $Al_{0.7}Li_{0.3}$ was assisted by selective oxidation of Li. The flame length was, in general, determined by the fuel and oxidizer diffusion rates. The lengths of flames containing actively burning metallic additives (i.e., mechanically alloyed $Al_{0.7}Li_{0.3}$ and nanocomposite 2B + Ti powders) were increased. This increase indicated an additional consumption of oxidizer in the jet's center, in which metallic particles were concentrated.

Acknowledgments

This work was supported in part the by Defense Threat Reduction Agency (DTRA), Award DAA30-1-9-0080, and the Office of Naval Research (ONR), Award N00014-00-1-0446. The interest and encouragement of W. Wilson and K. Kim of DTRA and J. Goldwasser of ONR [currently at the Defense Advanced Research Projects Agency (DARPA)] are gratefully acknowledged.

References

[1] Price, E. W., "Combustion of Metalized Propellants," *Progress in Astronautics and Aeronautics*, Vol. 90, 1984, pp. 479–513.

[2] Blomshield, F. S., Crump, J. E., Mathes, H. B., Stalnaker, R. A., and Beckstead, M. W., "Stability Testing of Full-Scale Tactical Motors," *Journal of Propulsion and Power*, Vol. 13, No. 3, 1997, pp. 349–355. doi:10.2514/2.5191

[3] Shalom, A., and Gany, A., "Flammability Limits and Ballistic Properties of Fuel-Rich Propellants," *Propellants, Explosives, Pyrotechnics*, Vol. 16, No. 2, 1991, pp. 59–64. doi:10.1002/prep.19910160204

[4] Kuzu, C., Ergin, H., Sözen, M. A., and Hüdaverdi, T., "Performance Investigation of Aluminised ANFO in Limestone Blasting Operations," *Mining Technology*, Vol. 114, No. 4, 2005, pp. 194–198. doi:10.1179/037178405X84805

[5] Dearden, P., "New Blast Weapons," *Journal of the Royal Army Medical Corps*, Vol. 147, No. 1, 2001, pp. 80–86.

[6] Roy, C. P., "Slurry Fuels," *Progress in Energy and Combustion Science*, Vol. 18, No. 5, 1992, pp. 409–427. doi:10.1016/0360-1285(92)90008-O

[7] Peleg, I., and Timnat, Y. M., "Investigation of Slurry Fuel Performance for Use in Ramjet Propulsors," *Israel Journal of Technology*, Vol. 20, Nos. 4–5, 1982, pp. 206–13.

[8] Wong, S.-C., and Lin, A.-C., "Microexplosion Mechanisms of Aluminum/Carbon Slurry Droplets," *Combustion and Flame*, Vol. 89, No. 1, 1992, pp. 64–76. doi:10.1016/0010-2180(92)90078-4

[9] Mueller, D. C., and Turns, S. R., "Some Aspects of Secondary Atomization of Aluminum/Hydrocarbon Slurry Propellants," *Journal of Propulsion and Power*, Vol. 9, No. 3, 1993, pp. 345–352. doi:10.2514/3.23628

[10] Pivkina, A., Ulyanova, P., Frolov, Y., Zavyalov, S., and Schoonman, J., "Nanomaterials for Heterogeneous Combustion," *Propellants, Explosives, Pyrotechnics*, Vol. 29, No. 1, 2004, pp. 39–49. doi:10.1002/prep.200400025

[11] Son, S. F., Foley, T. J., Sanders, V. E., Novak, A. M., Tasker, D. G., and Asay, B. W., "Overview of Nanoenergetic Material Research at Los Alamos," *Multifunctional Energetic Materials*, Materials Research Society Symposia Proceedings, Vol. 896, Materials Research Society, Warrendale, PA, 2006, pp. 87–98.

[12] Shoshin, Y. L., Mudryy, R. S., and Dreizin, E. L., "Preparation and Characterization of Energetic Al-Mg Mechanical Alloy Powders," *Combustion and Flame*, Vol. 128, No. 3, 2002, pp. 259–269. doi:10.1016/S0010-2180(01)00351-0

[13] Schoenitz, M., and Dreizin, E. L., "Structure and Properties of Al-Mg Mechanical Alloys," *Journal of Materials Research*, Vol. 18, No. 8, 2003, pp. 1827–1836. doi:10.1557/JMR.2003.0255

[14] Schoenitz, M., Ward, T. S., and Dreizin, E. L., "Fully Dense Nano-Composite Energetic Powders Prepared By Arrested Reactive Milling," *Proceedings of the Combustion Institute*, Vol. 30, 2005, pp. 2071–2078. doi:10.1016/j.proci.2004.08.134

[15] Schoenitz, M., Dreizin, E. L., and Shtessel, E., "Constant Volume Explosions of Aerosols of Metallic Mechanical Alloys and Powder Blends," *Journal of Propulsion and Power*, Vol. 19, No. 3, 2003, pp. 405–412. doi:10.2514/2.6144

[16] Shoshin, Y. L., and Dreizin, E. L., "Laminar Lifted Flame Speed Measurements for Aerosols of Metals and Mechanical Alloys," *AIAA Journal*, Vol. 42, No. 7, 2004, pp. 1416–1426. doi:10.2514/1.4772

[17] Shoshin, Y. L., Trunov, M. A., Zhu, X., Schoenitz, M., and Dreizin, E. L., "Ignition of Aluminum-Rich Al-Ti Mechanical Alloys in Air," *Combustion and Flame*, Vol. 144, No. 4, 2006, pp. 688–697. doi:10.1016/j.combustflame.2005.08.037

[18] Shoshin, Y., and Dreizin, E., "Production of Well-Controlled Laminar Aerosol Jets and Their Application for Studying Aerosol Combustion Processes," *Aerosol Science and Technology*, Vol. 36, 2002, pp. 953–962. doi:10.1080/02786820290092131

[19] Shoshin, Y., and Dreizin, E., "Particle Combustion Rates in Premixed Flames of Polydisperse Metal—Air Aerosols," *Combustion and Flame*, Vol. 133, 2003, pp. 275–287. doi:10.1016/S0010-2180(02)00571-0

[20] Trunov, M. A., Hoffmann, V. K., Schoentiz, M., and Dreizin, E. L., "Combustion of Boron-Titanium Nanocomposite Powders in Different Environments," *Journal of Propulsion and Power*, Vol. 24, No. 2, 2008, pp. 184–191. doi:10.2514/1.30483

[21] Zhu, X., Schoentiz, M., and Dreizin, E. L., "Mechanically Alloyed Al-Li Powders," *Journal of Alloys and Compounds*, Vol. 432, Nos. 1–2, 2007, pp. 111–115. doi:10.1016/j.jallcom.2006.05.114

[22] Zhu, X., "Synthesis and Characterization of Mechanically Alloyed Aluminum-Based Compounds as High Energy Density Materials," Ph.D. Dissertation, New Jersey Inst. of Technology, Newark, NJ, 2006.

[23] Lide, D. R. (ed.), *CRC Handbook of Chemistry and Physics*, 86th ed., Taylor and Francis, London, 2006.

[24] Willeke, K., and Baron, P. A., *Aerosol Measurements: Principles, Techniques, and Applications*, Van Nostrand Reinhold, New York, 1992.

[25] ImageTool, Software Package, Ver. 3.0, Univ. of Texas Health Science Center, San Antonio, TX, 2002.

[26] Tracker, Software Package, Ver. 3.0, NASA Lewis Research Center, Cleveland, OH, 1998.

[27] Larrabee, R. D., "The Spectral Emissivity and Optical Properties of Tungsten," Massachusetts Inst. of Technology, TR 328, Cambridge, MA, 1957, p. 81.

[28] *NIST Atomic Spectra Database* [online database], http://physics.nist.gov/PhysRefData/ASD/index.html [retrieved June 2006].

[29] Pearse, R. W. B., and Gaydon, A. G., *The Identification of Molecular Spectra*, 4th ed., Chapman and Hall, London, 1976.

[30] Chemical Equilibrium and Applications, Software Package, Ver. 2, NASA John H. Glenn Research Center at Lewis Field, Cleveland, OH, 1996.

[31] Zhao, Z., Li, J., Kazakov, A., Zeppieri, S. P., and Dryer, F. L., "Burning Velocities and a High-Temperature Skeletal Kinetic Model for *n*-Decane," *Combustion Science and Technology*, Vol. 177, No. 1, 2004, pp. 89–106. doi:10.1080/00102200590883769

[32] Turns, S. R., *An Introduction to Combustion: Concepts and Applications*, 2nd ed., McGraw-Hill, New York, 2000.

[33] Glassman, I., *Combustion*, 3rd ed., Academic Press, New York, 1996.

C. Avedisian
Associate Editor